

## **Automated whole-cell patch clamp electrophysiology of neurons *in vivo***

Suhasa B. Kodandaramaiah<sup>1,2</sup>, Giovanni Talei Franzesi<sup>1</sup>, Brian Y. Chow<sup>1</sup>, Edward S. Boyden<sup>1\*</sup>,  
Craig R. Forest<sup>2\*</sup>

<sup>1</sup>MIT Media Lab, McGovern Institute, Dept. of Biological Engineering, and Dept. of Brain and Cognitive Sciences, MIT, Cambridge, MA; <sup>2</sup>George W. Woodruff School of Mechanical Engineering, Georgia Institute Of Technology, Atlanta, GA

### **Correspondence to:**

Craig R. Forest  
Georgia Institute of Technology  
813 Ferst Dr, Room 411  
Atlanta, GA 30332  
Email: [cforest@gatech.edu](mailto:cforest@gatech.edu)  
Office phone: (404) 385-7645

and

Edward S. Boyden  
Massachusetts Institute of Technology  
E15-421  
20 Ames St.  
Cambridge, MA 02139  
Email: [esb@media.mit.edu](mailto:esb@media.mit.edu)  
Office phone: (650) 468-5625

**Abstract**

Whole-cell patch clamp electrophysiology of neurons is a gold standard technique for high-fidelity analysis of the biophysical mechanisms of neural computation and pathology but it requires great skill to perform. We have developed a robot that automatically performs patch clamping *in vivo*, algorithmically detecting cells by analyzing the temporal sequence of electrode impedance changes. We demonstrate good yield, throughput, and quality of automated intracellular recording in mouse cortex and hippocampus.

Whole-cell patch clamp recordings<sup>1,2</sup> of the electrical activity of neurons *in vivo* utilizes glass micropipettes to establish electrical and molecular access to the insides of neurons in intact tissue. This methodology exhibits signal quality and temporal fidelity sufficient to report the synaptic and ion-channel mediated subthreshold membrane potential changes that enable neurons to compute information, and that are affected in brain disorders or by drug treatment. In addition, molecular access to the cell enables infusion of dyes for morphological visualization, as well as extraction of cell contents for transcriptomic single-cell analysis<sup>3</sup>, which together enable the integrative analysis of molecular, anatomical, and electrophysiological properties of single cells in the intact brain. However, *in vivo* patching requires skill, being something of an art to perform, and is laborious. This has posed a challenge for its broad adoption in neuroscience and biology, and precluded systematic or scalable *in vivo* experiments.

We have discovered that unbiased, non-image-guided, *in vivo* whole-cell patching ('blind' patch clamping) of neurons (**Fig. 1a**), in which micropipettes are lowered until a cell is detected and then an opening in the cell membrane created for intracellular recording, can be reduced to a reliable algorithm. The patch algorithm takes place in four stages (**Fig. 1a**): "regional pipette localization," in which the pipette is rapidly lowered to a desired depth under positive pressure; "neuron hunting," in which the pipette is advanced more slowly at lower pressure until a neuron is detected, as reflected by a specific temporal sequence of electrode impedance changes; "gigaseal formation," in which the pipette is hyperpolarized and suction applied to create the gigaseal; and "break-in," in which a brief voltage pulse ("zap") is applied to the cell to establish the whole cell state. We constructed a simple automated robot to perform this algorithm (**Fig. 1b**), which actuates a set of motors and valves rapidly upon recognition of specific temporal sequences of microelectrode impedance changes, achieving *in vivo* patch clamp recordings in a total period of 3-7 minutes of robot operation. The robot is relatively inexpensive, and can easily be appended to an existing patch rig. We demonstrate the utility of this autopatching robot in obtaining high-quality recordings, which could be held for an hour or longer, in the cortex and hippocampus of anesthetized mouse brain.

The robot (**Fig. 1b**) monitors pipette resistance as the pipette is lowered into the brain, and automatically moves the pipette in incremental steps via a linear actuator. In principle, the pipette resistance monitoring can be performed by a traditional patch amplifier and digitizer, and the 3 axis linear actuator typically used for *in vivo* patching can be used as the robotic actuator; we here

for flexibility added an additional computer interface board to support pipette resistance monitoring, and an additional linear actuator for pipette movement. The robot also contains a set of valves connected to pressure reservoirs to provide positive pressure during pipette insertion into the brain, as well as negative pressure as necessary to result in gigaseal formation and attainment of the whole cell state (see **Supplementary Fig. 1** for details).

The algorithm derivation took place in the cortex, and the validation of the algorithm then took place in both cortex and hippocampus, to confirm generality. After the “regional pipette localization” stage, pipettes that undergo increases of resistance of greater than 300 k $\Omega$  after this descent to depth are rejected, which greatly increases the yield of later steps (**Supplementary Note 1**). During “neuron hunting,” the key indicator of neuron presence is that as the pipette is lowered into the brain in a stepwise fashion, there is a monotonic increase in pipette resistance across several consecutive steps (e.g., a 200-250 k $\Omega$  increase in pipette resistance across three 2  $\mu$ m steps). Successfully detected neurons also exhibited an increase in heartbeat modulation of the pipette current (**Supplementary Fig. 2**, as has been noted before<sup>2</sup>, although we did not utilize this in our current version of the algorithm due to the variability in the shape and frequency of the heartbeat from cell to cell (**Supplementary Note 1**). “Gigaseal formation” was implemented as a simple feedback loop, introducing negative pressure and hyperpolarization of the pipette as needed to form the seal. Finally, “break-in” was implemented through the application of suction and the application of a “zap” voltage pulse to enable the whole-cell state. Information about the algorithm are indicated in **Online Methods, Supplementary Fig. 3 and Supplementary Note 1**. Detailed instructions for robot construction are described in **Supplementary Software (Autopatcher User Manual)**.

We validated the algorithm and robot on targets within the cortex and hippocampus of anesthetized mice. The robot running the algorithm (**Fig. 1a, b, Supplementary Fig. 3**), obtained successful whole-cell patch recordings 32.9% of the time (**Supplementary Table 1**; defined as < 500 pA of current when held at – 65 mV, for at least 5 minutes;  $n = 24$  out of 73 attempts), and successful gigaseal cell-attached patch clamp recording 36% of the time (defined as a stable seal of >1 G $\Omega$  resistance;  $n = 27$  out of 75 attempts), success rates that are similar to, or exceed, those of a trained investigator manually performing blind whole-cell patch clamping *in vivo* (for us, 28.8% success at whole-cell patching;  $n = 17$  out of 59 fully manual attempts; see also refs. <sup>2,4,5</sup>). Example traces from neurons autopatched in cortex and hippocampus are shown in **Fig. 1c,d**. When biocytin was included in the pipette solution, morphologies of cells could be visualized (**Fig. 1e** and

**Supplementary Fig. 4)** histologically. Focusing on the robot’s performance after the “regional pipette localization” stage (i.e., leaving out losses due to pipette blockage during the descent to depth), the autopatcher was successful at whole-cell patch clamping 43.6% of the time (**Supplementary Table 1**;  $n = 24$  out of 55 attempts starting with the “neuron hunting” stage), and at gigaseal cell-attached patch clamping 45.8% of the time ( $n = 27$  out of 59 attempts). Of the successful recordings described in the previous paragraph, approximately 10% were putative glia, as reflected by their capacitance and lack of spiking<sup>6</sup> (4 out of 51 successful autopatched recordings; 2 out of 17 successful fully manual recordings). For simplicity, we analyzed just the neurons, in the rest of the paper; their various firing patterns are described in the **Supplementary Note 2**. From the beginning of the neuron-hunting stage, to acquisition of successful whole-cell or gigaseal cell-attached recordings, took  $5 \pm 2$  minutes for the robot to perform (**Supplementary Table 1**), not significantly different from the duration of fully manual patching ( $5 \pm 3$  minutes;  $p = 0.7539$ ;  $n = 47$  autopatched neurons, 15 fully manually patched neurons).

A representative autopatcher run, plotting the pipette resistance versus time, is shown in **Fig. 2a**, with key events indicated by Roman numerals; raw current traces resulting from the continuously applied voltage pulses, from which the pipette resistances were derived, are shown in **Fig. 2b**. Note the small visual appearance of the change in pipette currents observed when a neuron is detected (**Fig. 2b**, event ii). See **Online methods** for details of the autopatcher timecourse and execution. The quality of cells recorded by the autopatcher was comparable to those in published studies conducted by skilled human investigators<sup>2, 4, 7-9</sup>, and to our own fully manually patched cells (**Fig. 2c-f**, **Supplementary Fig. 5**). These comparisons showed no statistically significant difference between  $n = 23$  auto-whole-cell patched and  $n = 15$  fully manually patched neurons for access resistance, holding current, resting membrane potential, holding time, gigaseal resistance, cell membrane capacitance, or cell membrane resistance (detailed statistics in **Supplementary Notes 3 and 4**).

Once the robot has been assembled, it is easy to use it to derive alternative or specialized algorithms (e.g., if a specialized cell type is the target, or if image-guided or other styles of patching is desired, or if the technology is desired to be combined with other technologies such as optogenetics for cell-type identification<sup>10</sup>). As an example, we derived a variant of the algorithm that uses pulses of suction to break in to cells, rather than “zap” (**Supplementary Fig. 6**); the yields, cell qualities, and cell properties obtained by the suction-pulse variation of the autopatch algorithm were comparable to those obtained by the original algorithm (**Supplementary Fig. 7**).

The inherent data logging of the robot allows fine-scale analyses of the patch process, for example revealing that the probability of success of autopatching starts at 50-70% in the first hour, and then drops to 20-50% over the next few hours, presumably due to cellular displacement intrinsic to the *in vivo* patching process (**Supplementary Fig. 7d**).

We have developed a robot that automatically performs patch clamping *in vivo*, algorithmically detecting cells by analyzing the temporal sequence of electrode impedance changes, and demonstrated it in the cortex and hippocampus of live mice. We anticipate that other applications of robotics to the automation of *in vivo* neuroscience experiments, and to other *in vivo* assays in bioengineering and medicine, will be possible. The ability to automatically make micropipettes in a high-throughput fashion<sup>11</sup>, and to install them automatically, might eliminate some of the few remaining steps requiring human intervention. The use of automated respiratory and temperature monitoring could enable a single human operator to control many rigs at once, increasing throughput further (see **Supplementary Note 5** for discussion of throughput). As a final example, the ability to control many pipettes within a single brain, and to perform parallel recordings of neurons within a single brain region, may open up new strategies for understanding how different cell types function in the living milieu.

### **Acknowledgments**

We would like to acknowledge electronic switch design by G. Holst at Georgia Tech. E.S.B. acknowledges funding by the National Institute of Health (NIH) Director's New Innovator Award (DP2OD002002) and the NIH EUREKA Award program (1R01NS075421) and other NIH Grants, the National Science Foundation (NSF) CAREER award (CBET 1053233) and other NSF Grants, Jerry and Marge Burnett, Google, Human Frontiers Science Program, MIT McGovern Institute and the McGovern Institute Neurotechnology Award Program, MIT Media Lab, NARSAD, Paul Allen Distinguished Investigator Award, Alfred P. Sloan Foundation, and the Wallace H. Coulter Foundation. C.R.F acknowledges funding by the NSF (CISE 1110947, EHR 0965945) as well as American Heart Association (10GRNT4430029), the Georgia Economic Development Association, the Wallace H. Coulter Foundation, Center for Disease Control, NSF National Nanotechnology Infrastructure Network (NNIN), and from Georgia Tech: Institute for BioEngineering and BioSciences Junior Faculty Award, Technology Fee Fund, Invention Studio, and the George W. Woodruff School of Mechanical Engineering.

## Authors' Contributions

S.B.K., B.Y.C, E.S.B. and C.R.F. designed devices and experiments and wrote the paper. S.B.K. conducted experiments. G.T.F. assisted with experiments and autopatcher pilot testing.

## Competing financial interests

The authors declare no competing financial interests.

## Figure Legends

**Figure 1. The autopatcher: a robot for *in vivo* patch clamping.** (a) The four stages of the automated *in vivo* patch algorithm (detailed in **Supplementary Fig. 3**). (b) Schematic of a simple robotic system capable of performing the autopatching algorithm, consisting of a conventional *in vivo* patch setup, equipped with a programmable linear motor (note that if the vertical axis of the 3 axis linear actuator is computer-controlled, this can be omitted), a controllable bank of pneumatic valves for pressure control, and a secondary computer interface board (if the patch amplifier provides direct access to these measurements, this can be omitted). (c) Current clamp traces during current injection (*top*; 2 s-long pulses of  $-60$ ,  $0$ , and  $+80$  pA current injection), and at rest (*bottom*; note compressed timescale relative to the top trace), for an autopatched cortical neuron. Access resistance,  $44\text{ M}\Omega$ ; input resistance,  $41\text{ M}\Omega$ ; depth of cell  $832\text{ }\mu\text{m}$  below brain surface. (d) Current clamp traces during current injection (*top*; 2 s-long pulses of  $-60$ ,  $0$ , and  $+40$  pA current injection), and at rest (*bottom*), for an autopatched hippocampal neuron. Access resistance,  $55\text{ M}\Omega$ ; input resistance,  $51\text{ M}\Omega$ ; depth of cell,  $1,320\text{ }\mu\text{m}$ . (e) Biocytin fill of a representative autopatched cortical pyramidal neuron. Scale bar,  $50\text{ }\mu\text{m}$ .

**Figure 2. Autopatcher operation and performance.** (a) Representative timecourse of pipette resistance during autopatcher operation, *top*, with zoomed-in view of the neuron hunting phase, *bottom*. Roman numerals: i, the first of the series of resistance measurements that indicate neuron detection; ii, the last of the series; iii, when positive pressure is released; iv, when suction is applied; v, when holding potential starts to ramp from  $-30\text{ mV}$  to  $-65\text{ mV}$ ; vi, when it hits  $-65\text{ mV}$ ; vii, break-in. (b) Raw traces showing patch pipette currents, while a square voltage wave ( $10\text{ Hz}$ ,  $10\text{ mV}$ ) is applied, at the events flagged by Roman numerals in **Fig. 2a**. (c-f) Quality of recordings obtained with the autopatcher vs. by manual whole cell patch clamping. (c) *left*, Plot of access resistances obtained versus pipette depth and *right*, bar graph summary of access resistances (mean  $\pm$  s.d.), for the final autopatcher whole cell patch validation test set (closed symbols;  $n = 23$ ), the test set in which the autopatcher concludes in the gigaseal state (open symbols,  $n = 24$ ;

data acquired after manual break-in), and the test set acquired via manual whole cell patch clamp (grayed symbols;  $n = 15$ ), for cortical (circles) and hippocampal (triangles) neurons. **(d)** *left*, Resting potential versus pipette depth, and *right*, summary data, plotted as in **c**. **(e)** *left*, Holding current versus pipette depth, and *right*, summary, plotted as in **c**. **(f)** *left*, Holding times versus pipette depth, and *right*, summary, plotted as in **c** (including recordings that were deliberately terminated, as well as recordings terminated spontaneously).

## Online Methods

### Surgical procedures.

All animal procedures were approved by the Massachusetts Institute of Technology (MIT) Committee on Animal Care. Adult male C57BL/6 mice, 8-12 weeks old, were purchased from Taconic. Upon arrival, the mice were housed in standard cages in the MIT animal facility with ad libitum food and water in a controlled light-dark cycle environment, with standard monitoring by veterinary staff, for the period before the experiment. On the day of the experiment, they were anesthetized using ketamine/xylazine (initially at 100 mg/kg and 10 mg/kg, and redosed at 30-45 minute intervals with 10-15% of the initial ketamine dose as needed, using toe pinch reflex as a standard metric of anesthesia depth). The scalp was shaved, and the mouse placed in a custom stereotax, with ophthalmic ointment applied to the eyes, and with Betadine and 70% ethanol used to sterilize the surgical area. Three self-tapping screws (F000CE094, Morris Precision Screws and Parts) were attached to the skull and a plastic headplate affixed using dental acrylic, as previously described<sup>12</sup>. Once set (~20 minutes), the mice were removed from the stereotactic apparatus and placed in a custom-built low profile holder. A dental drill was used to open up one or more craniotomies (1-2 mm diameter) by thinning the skull until ~100  $\mu\text{m}$  thick, and then a small aperture was opened up with a 30 gauge needle tip. Cortical craniotomies occurred at stereotaxic coordinates: anteroposterior, 0 mm relative to bregma; mediolateral, 0-1 mm left or right of the midline; neuron hunting began at 400  $\mu\text{m}$  depth. Hippocampal craniotomies occurred at stereotaxic coordinates: anteroposterior, -2 mm relative to bregma; mediolateral, 0.75-1.25 mm left or right of the midline; neuron hunting began at 1100  $\mu\text{m}$  depth. It is critical to ensure that bleeding is minimal and the craniotomy is clean, as this allows good visualization of the pipette, and minimizes the number of pipettes blocked after insertion into the brain. The dura was removed using a pair of fine forceps. The craniotomy was superfused with artificial cerebrospinal fluid (ACSF, consisting of 126 mM NaCl, 3 mM KCl, 1.25 mM  $\text{NaH}_2\text{PO}_4$ , 2 mM



CaCl<sub>2</sub>, 2 mM MgSO<sub>4</sub>, 24 mM NaHCO<sub>3</sub>, and 10 mM glucose), to keep the brain moist until the moment of pipette insertion.

17 mice were used to derive the autopatching algorithm (**Supplementary Fig. 2**). 16 mice were used to validate the robot for the primary test-set (**Fig. 2, Supplementary Fig. 3a and Supplementary Fig. 3b**). For the manual experiments (**Fig. 2c-f and Supplementary Fig. 3c**), we used 4 mice. For the development of the suction-based autopatching variant (**Supplementary Fig. 5, 6**), we used 5 mice. Out of the 5 mice used for suction-based autopatching, 3 mice were used for the throughput estimations (**Supplementary Note 6**). For biocytin filling experiments (**Fig. 1f and Supplementary Fig. 4**) and validation of heartbeat modulation as a method for confirming neuronal detection (**Supplementary Note 1**), we used 6 additional mice.

At the end of the patch clamp recording, mice were euthanized, while still fully anesthetized, via cervical dislocation, unless biocytin filling was attempted. In the case of biocytin filling, the mice were isoflurane anesthetized, then transcardially perfused in 4% ice-cold through the left cardiac ventricle with ~40 mL of ice-cold 4% paraformaldehyde in phosphate buffered saline (PBS) (see **Histology and Imaging** section for more details).

### **Electrophysiology.**

Borosilicate glass pipettes (Warner) were pulled using a filament micropipette puller (Flaming-Brown P97 model, Sutter Instruments), within a few hours before beginning the experiment, and stored in a closed petri dish to reduce dust contamination. We pulled glass pipettes with resistances between 3-9 MΩ. The intracellular pipette solution consisted of (in mM): 125 potassium gluconate (with more added empirically at the end, to bring osmolarity up to ~290 mOsm), 0.1 CaCl<sub>2</sub>, 0.6 MgCl<sub>2</sub>, 1 EGTA, 10 HEPES, 4 Mg ATP, 0.4 Na GTP, 8 NaCl (pH 7.23, osmolarity 289 mOsm), similar as to what has been used in the past<sup>13</sup>. For experiments with biocytin, 0.5% biocytin (weight/volume) was added to the solution before the final gluconate-based osmolarity adjustment, and osmolarity then adjusted (to 292 mOsm) with potassium gluconate. We performed manual patch clamping using previously described protocols<sup>2,9</sup>, with some modifications and iterations as explained in the text, in order to prototype algorithm steps and to test them.

### **Robot construction.**

We assembled the autopatcher (**Fig. 1b,c**) through modification of a standard *in vivo* patch clamping system. The standard system comprised a 3-axis linear actuator (MC1000e, Siskiyou Inc) for holding the patch headstage, and a patch amplifier (Multiclamp 700B, Molecular Devices) that connects its patch headstage to a computer through an analog/digital interface board (Digidata 1440A, Molecular Devices). For programmable actuation of the pipette in the vertical direction, we mounted a programmable linear motor (PZC12, Newport) onto the 3-axis linear actuator. For experiments where we attempted biocytin filling, we mounted the programmable linear motor at a 45° angle to the vertical axis, to reduce the amount of background staining in the coronal plane that we did histological sectioning along. The headstage was in turn mounted on the programmable linear motor through a custom mounting plate. The programmable linear motor was controlled using a motor controller (PZC200, Newport Inc) that was connected to the computer through a serial COM port. An additional data acquisition (DAQ) board (USB 6259 BNC, National Instruments Inc) was connected to the computer via a USB port, and to the patch amplifier through BNC cables, for control of patch pipette voltage commands, and acquisition of pipette current data, during the execution of the autopatcher algorithm. During autopatcher operation, the USB 6259 board sent commands to the patch amplifier; after acquisition of cell-attached or whole-cell-patched neurons, the patch amplifier would instead receive commands from the Digidata; we used a software-controlled TTL co-axial BNC relay (CX230, Tohtsu) for driving signal switching between the USB 6259 BNC and the Digidata, so that only one would be empowered to command the patch amplifier at any time. The patch amplifier streamed its data to the analog input ports of both the USB DAQ and the Digidata throughout and after autopatching. For pneumatic control of pipette pressure, we used a set of three solenoid valves (2-input, 1-output, LHDA0533215H-A, Lee Company). They were arranged, and operated, in the configuration shown in **Supplementary Fig. 1**. The autopatcher program was coded in, and run by, Labview 8.6 (National Instruments). Detailed instructions for robot construction are described in the **Supplementary Software (Autopatcher User Manual)**.

The USB6259 DAQ sampled the patch amplifier at 30 KHz and with unity gain applied, and then filtered the signal using a moving average smoothing filter (half width, 6 samples, with triangular envelope), and the amplitude of the current pulses was measured using the peak-to-peak measurement function of Labview. During the entire procedure, a square wave of voltage was applied, 10 mV in amplitude, at 10 Hz, to the pipette via the USB6259 DAQ analog output. Resistance values were then computed, by dividing applied voltage by the peak-to-peak current observed, for 5 consecutive voltage pulses, and then these 5 values were averaged. Once the

autopatcher process was complete, neurons were recorded using Clampex software (Molecular Devices). Signals were acquired at standard rates (e.g., 30-50 KHz), and low-pass filtered (Bessel filter, 10 KHz cutoff). All data was analyzed using Clampfit software (Molecular Devices) and MATLAB (Mathworks).

### **Robot Operation.**

At the beginning of the experiment, we installed a pipette and filled it with pipette solution using a thin polyimide/fused silica needle (Microfil) attached to a syringe filter (0.2  $\mu\text{m}$ ) attached to a syringe (1 mL). We removed excess ACSF to improve visualization of the brain surface in the pipette lowering stage, and then applied positive pressure (800-1000 mBar), low positive pressure (25-30 mBar), and suction pressure (-15 to -20 mBar) at the designated ports (**Fig. 1, Supplementary Fig. 1**) and clamped the tubing to the input ports with butterfly clips; the initial state of high positive pressure was present at this time (with all valves electrically off). We used the 3-axis linear actuator (Siskiyou) to manually position the pipette tip over the craniotomy using a control joystick with the aid of a stereomicroscope (Nikon). The pipette was lowered until it just touched the brain surface (indicated by dimpling of surface) and retracted back by 20-30 micrometers. The autopatcher software then denotes this position, just above the brain surface, as  $z = 0$  for the purposes of executing the algorithm (**Supplementary Fig. 2**), acquiring the baseline value  $R(0)$  of the pipette resistance at this time (the z-axis is the vertical axis perpendicular to the earth's surface, with greater values going downwards). The pipette voltage offset was automatically nullified by the "pipette offset" function in the Multiclamp Commander (Molecular Devices). We ensured that electrode wire in the pipette was chlorided enough so as to minimize pipette current drift which can affect the detection of the small resistance measurements that occur during autopatcher operation. The brain surface was then superfused with ACSF and the autopatcher program was started. See included **Supplementary Software (Autopatcher User Manual)** for detailed description of running the Labview program for autopatching. Updated versions of the software and user manual will be made available online at <http://autopatcher.org>.

### **Details of Autopatcher Program Execution.**

The autopatcher evaluates the pipette electrical resistance is evaluated outside the brain (e.g., between 3-9  $\text{M}\Omega$  is typical) for 30-60 seconds to see if AgCl pellets or other particulates internally clog the pipette (indicated by increases in resistance). If the pipette resistance remains

constant and is of acceptable resistance, the Autopatcher program is started. The program records the resistance of the pipette outside the brain and automatically lowers the pipette to a pre-specified target region within the brain (the stage labeled “regional pipette localization” in **Fig. 1a**), followed by a second critical examination of the pipette resistance for quality control. This check is followed by an iterative process of lowering the pipette by small increments, while looking for a pipette resistance change indicative of proximity to a neuron suitable for recording (the “neuron hunting” stage). During this stage, the robot looks for a specific sequence of resistance changes that indicates that a neuron is proximal, attempting to avoid false positives that would waste time and decrease cell yield. After detecting this signature, the robot halts movement, and begins to actuate suction and pipette voltage changes so as to form a high-quality seal connecting the pipette electrically to the outside of the cell membrane (the “gigaseal formation” stage), thus resulting in a gigaseal cell-attached recording. If whole-cell access is desired, the robot can then be used to perform controlled application of suction in combination with brief electrical pulses to break into the cell (the “break-in” stage, **Supplementary Fig. 3**). Alternately, break-in can also be achieved using pulses of suction (**Supplementary Fig. 6**).

Throughout the process, the robot applies a voltage square wave to the pipette (10 Hz, 10 mV alternating with 0 mV relative to pipette holding voltage), and the current is measured, in order to calculate the resistance of the pipette at a given depth or stage of the process. Throughout the entire process of robot operation, this pipette resistance is the chief indicator of pipette quality, cell presence, seal quality, and recording quality, and the algorithm attempts to make decisions – such as whether to advance to the next stage, or to restart a stage, or to halt the process – entirely on the temporal trajectory taken by the pipette resistance during the experiment. The performance of the robot is enabled by two critical abilities of the robot: its ability to monitor the pipette resistance quantitatively over time, and its ability to execute actions in a temporally precise fashion upon the measured pipette resistance reaching quantitative milestones.

Focusing on the data for the  $n = 47$  neurons in the main validation test set: the neuron-hunting stage took on average  $2.5 \pm 1.7$  minutes ( $n = 47$ ), with the time to find a target that later led to successful gigaseal not differing significantly from the time to find a target that does not lead to a gigaseal ( $P = 0.8114$ ; t-test;  $n = 58$  unsuccessful gigaseal formation trials), that is, failed trials did not take longer than successful ones. The gigaseal formation took  $2.6 \pm 1.0$  minutes, including for the whole cell autopatched case the few seconds required for break-in; failed attempts to form gigaseals were truncated at the end of the ramp down procedure and thus took

~85 seconds. These durations are similar to those obtained by trained human investigators practicing published protocols<sup>4</sup>.

**Histology and Imaging.** For experiments with biocytin filling of cells, mice were perfused through the left cardiac ventricle with ~40 mL of ice-cold 4% paraformaldehyde in phosphate buffered saline (PBS) while anesthetized with isoflurane. Perfused brains were then removed from the skull then postfixed overnight in the same solution at 4 °C. The fixed brains were incubated in 30% sucrose solution for 2 days until cryoprotected (i.e., the brains sank). The brains were flash frozen in isopentane cooled using dry ice at temperatures between -30 °C to -40 °C. The flash frozen brains were mounted on mounting plates using OCT as base, and covered with tissue embedding matrix to preserve tissue integrity, and 40 µm thick slices were cut at -20 °C using a cryostat (Leica). The brain slices were mounted on charged glass slides (e.g., SuperFrost) and incubated at room temperature for 4 hours in PBS containing 0.5% Triton-X (vol/vol) and 2% goat serum (vol/vol). This was followed by 12-14 hours of incubation at 4 °C in PBS containing 0.5% Triton-X (vol/vol), 2% goat serum (vol/vol) and Alexa 594 conjugated with streptavidin (Life Technologies, diluted 1:200). After incubation, the slices were thoroughly washed in PBS containing 100 mM glycine and 0.5% Triton-X (vol/vol) followed by washing in PBS with 100 mM glycine. Slices were then mounted in Vectashield with DAPI (Vector Labs), covered using a coverslip, and sealed using nail polish. Image stacks were obtained using a confocal microscope (Zeiss) with 20x objective lens. Maximum intensity projections of the image stacks were taken using ImageJ software. If needed to reconstruct full neuron morphology, multiple such maximum intensity projection images were auto-leveled, then montaged, using Photoshop CS5 software.

**Supplementary  
File**

**Supplementary  
Figure 1**

**Supplementary  
Figure 2**

**Supplementary  
Figure 3**

**Title**

Details of Autopatcher setup

Raw current traces recorded during  
“neuron hunting” stage.

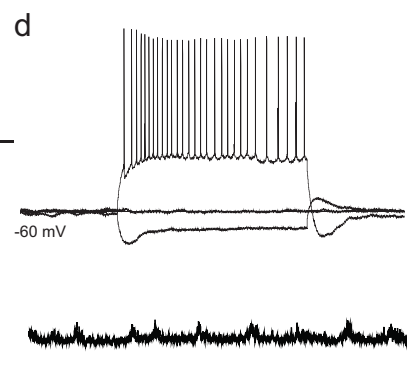
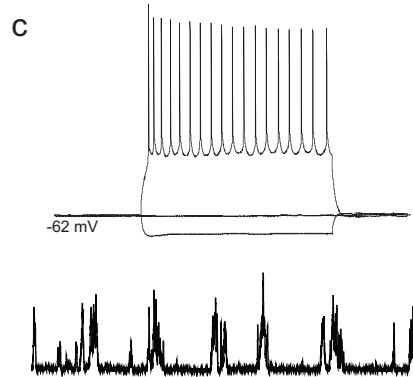
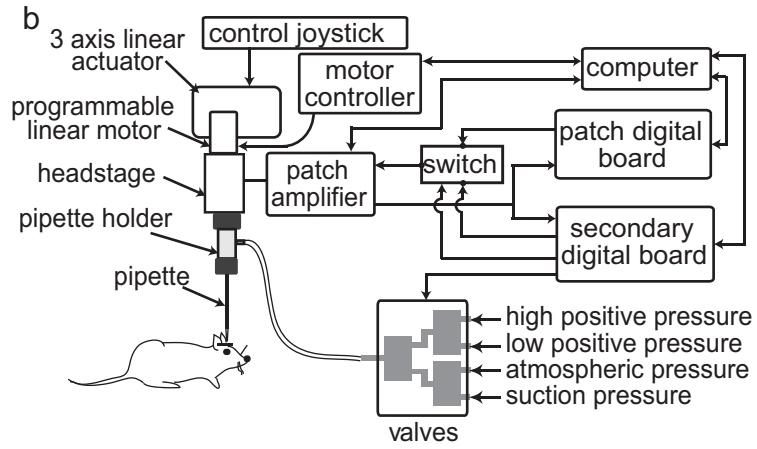
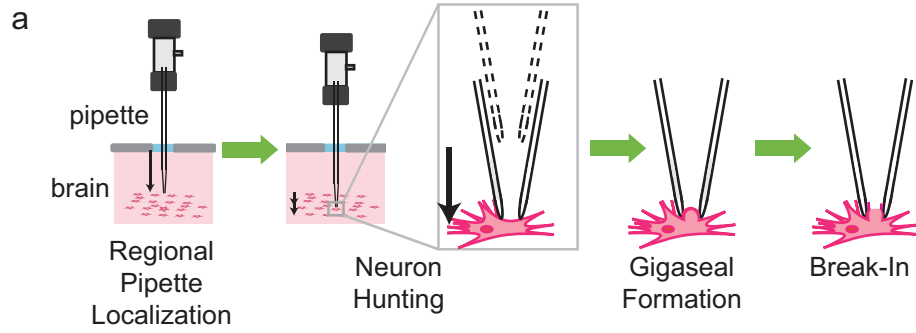
The full algorithm for automated *in vivo*  
patch clamping using suction with ‘zap’  
function for breaking in

<b>Supplementary Figure 4</b>	Neurons filled with biocytin, and visualized with Alexa 594-streptavidin, after recording by the autopatching robot.
<b>Supplementary Figure 5</b>	Cell characteristics after completion of autopatching or manual patching using the algorithm of Supplementary Fig. 2.
<b>Supplementary Figure 6</b>	The algorithm of Supplementary Fig. 2, modified to use suction pulses instead of “zap”, to break in.
<b>Supplementary Figure 7</b>	Quality of recordings obtained using the autopatcher using the ‘suction pulses’ method for break-in and achieving the whole cell state, as described in Supplementary Fig. 5.
<b>Supplementary Table 1</b>	Autopatcher performance
<b>Supplementary Note 1</b>	Derivation of the autopatcher algorithm: principles of whole cell patch clamp <i>in vivo</i>
<b>Supplementary Note 2</b>	The cell types patched by the autopatcher
<b>Supplementary Note 3</b>	Statistics for evaluation of cell quality, for autopatched neurons
<b>Supplementary Note 4</b>	Statistics for comparing cell quality of autopatched neurons with fully manual patched neurons
<b>Supplementary Note 5</b>	Thoughts on throughput of the autopatcher
<b>Supplementary Software</b>	Autopatcher labview software and Autopatcher User Manual

## REFERENCES FOR THE ONLINE METHODS SECTION

1. Hamill, O.P., Marty, A., Neher, E., Sakmann, B. & Sigworth, F.J. Improved patch-clamp techniques for high-resolution current recording from cells and cell-free membrane patches. *Pflugers Arch* **391**, 85-100 (1981).
2. Margrie, T.W., Brecht, M. & Sakmann, B. In vivo, low-resistance, whole-cell recordings from neurons in the anaesthetized and awake mammalian brain. *Pflugers Arch* **444**, 491-498 (2002).
3. Eberwine, J. et al. Analysis of gene expression in single live neurons. *Proc Natl Acad Sci USA* **89**, 3010-3014 (1992).
4. Lee, A.K., Epsztein, J. & Brecht, M. Head-anchored whole-cell recordings in freely moving rats. *Nat. Protocols* **4**, 385-392 (2009).
5. Kitamura, K., Judkewitz, B., Kano, M., Denk, W. & Hausser, M. Targeted patch-clamp recordings and single-cell electroporation of unlabeled neurons in vivo. *Nat Meth* **5**, 61-67 (2008).
6. Trachtenberg, M.C. & Pollen, D.A. Neuroglia: Biophysical Properties and Physiologic Function. *Science* **167**, 1248-1252 (1970).
7. Harvey, C.D., Collman, F., Dombeck, D.A. & Tank, D.W. Intracellular dynamics of hippocampal place cells during virtual navigation. *Nature* **461**, 941-946 (2009).
8. DeWeese, M.R. & Zador, A.M. Non-Gaussian membrane potential dynamics imply sparse, synchronous activity in auditory cortex. *J Neurosci* **26**, 12206-12218 (2006).
9. DeWeese, M.R. Whole-cell recording in vivo. *Curr Protoc Neurosci* **Chapter 6**, Unit 6 22 (2007).
10. Boyden, E.S. A history of optogenetics: the development of tools for controlling brain circuits with light. *F1000 Biology Reports* **3** (2011).
11. Pak, N., Dergance, M.J., Emerick, M.T., Gagnon, E.B. & Forest, C.R. An Instrument for Controlled, Automated Production of Micrometer Scale Fused Silica Pipettes. *Journal of Mechanical Design* **133**, 061006 (2011).
12. Boyden, E.S. & Raymond, J.L. Active reversal of motor memories reveals rules governing memory encoding. *Neuron* **39**, 1031-1042 (2003).
13. Chow, B.Y. et al. High-performance genetically targetable optical neural silencing by light-driven proton pumps. *Nature* **463**, 98-102 (2010).

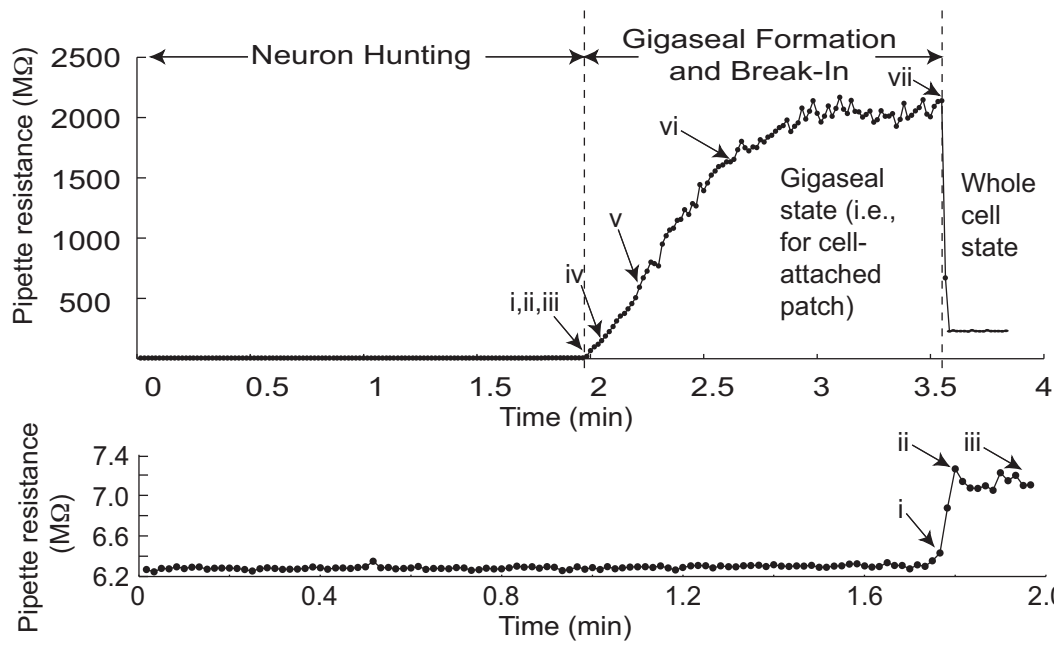




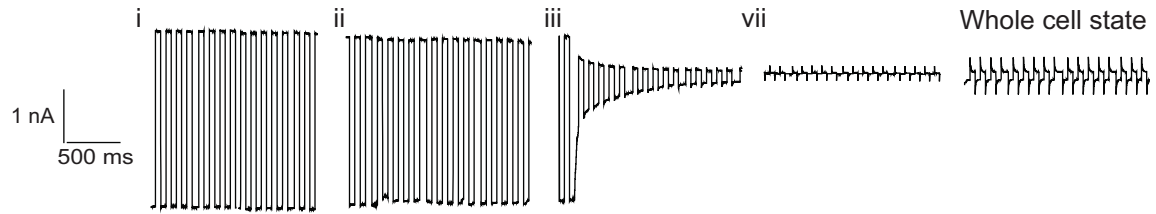


a

Timecourse of autopatching algorithm



b

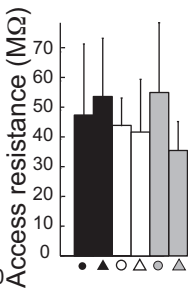
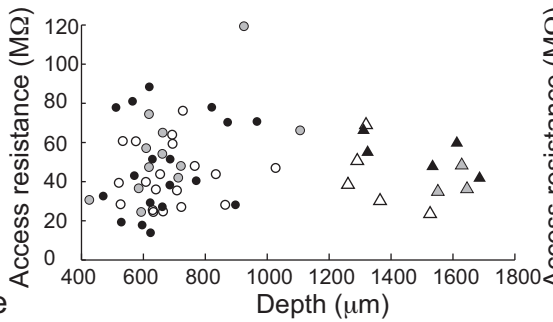


Quality of obtained recordings

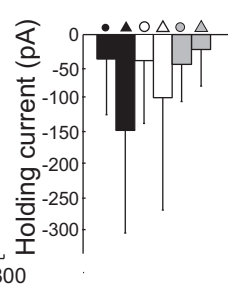
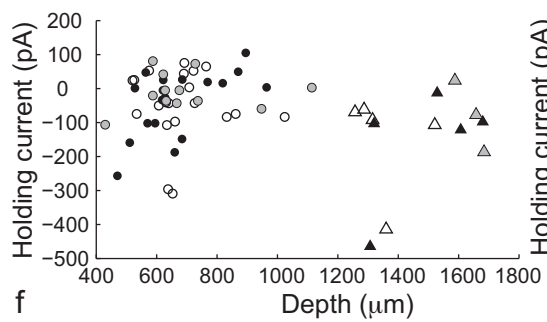
cortex hippocampus

algorithm ends in whole cell state ● ▲  
 algorithm ends in gigaseal state (manual break-in) ○ △  
 manual whole cell patch clamping ◐ ◑

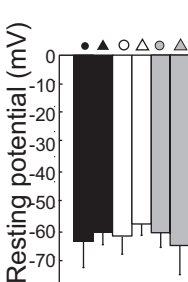
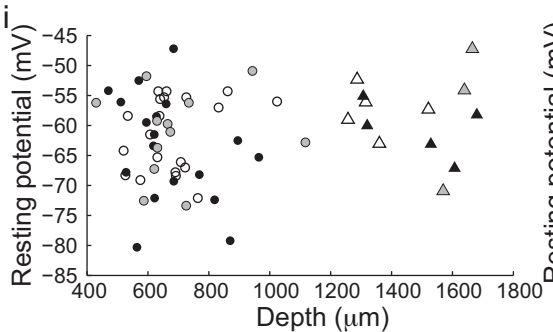
c



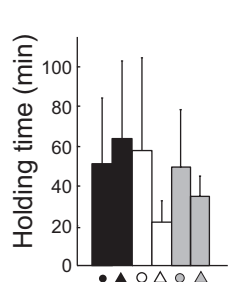
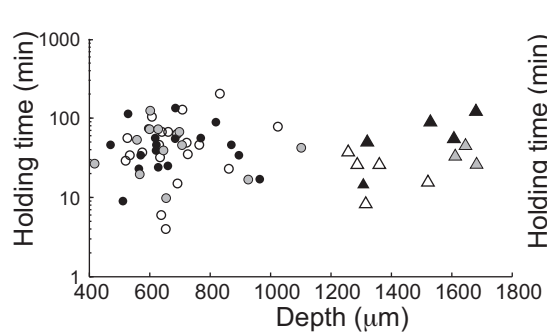
d

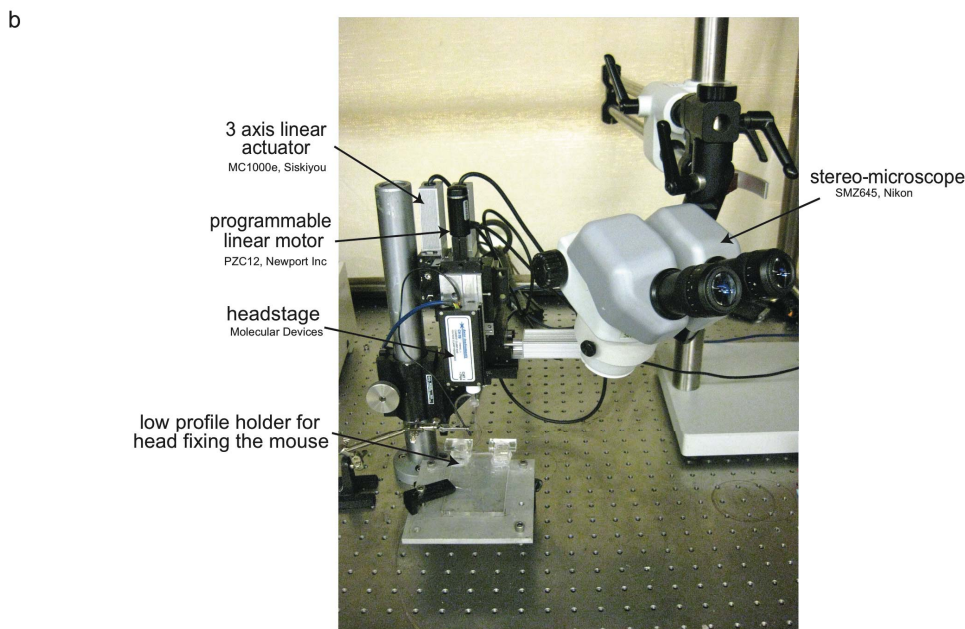
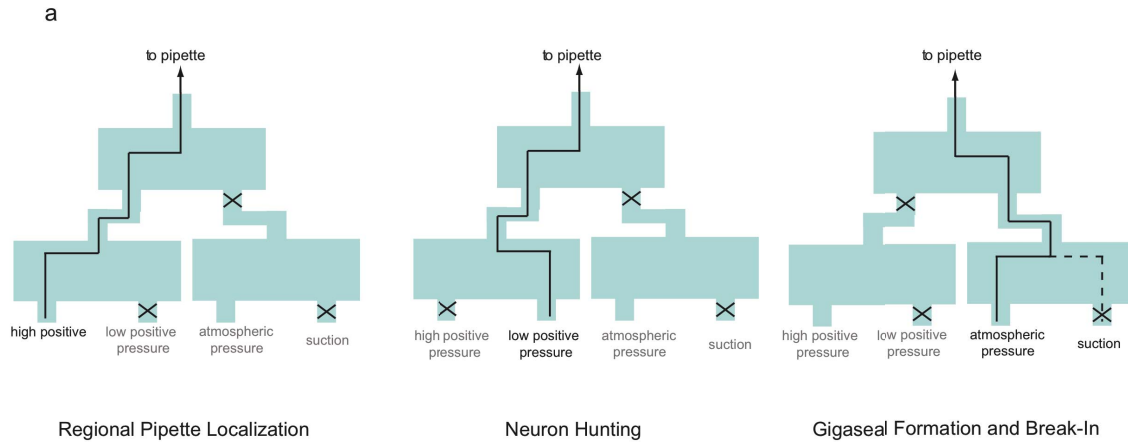


e

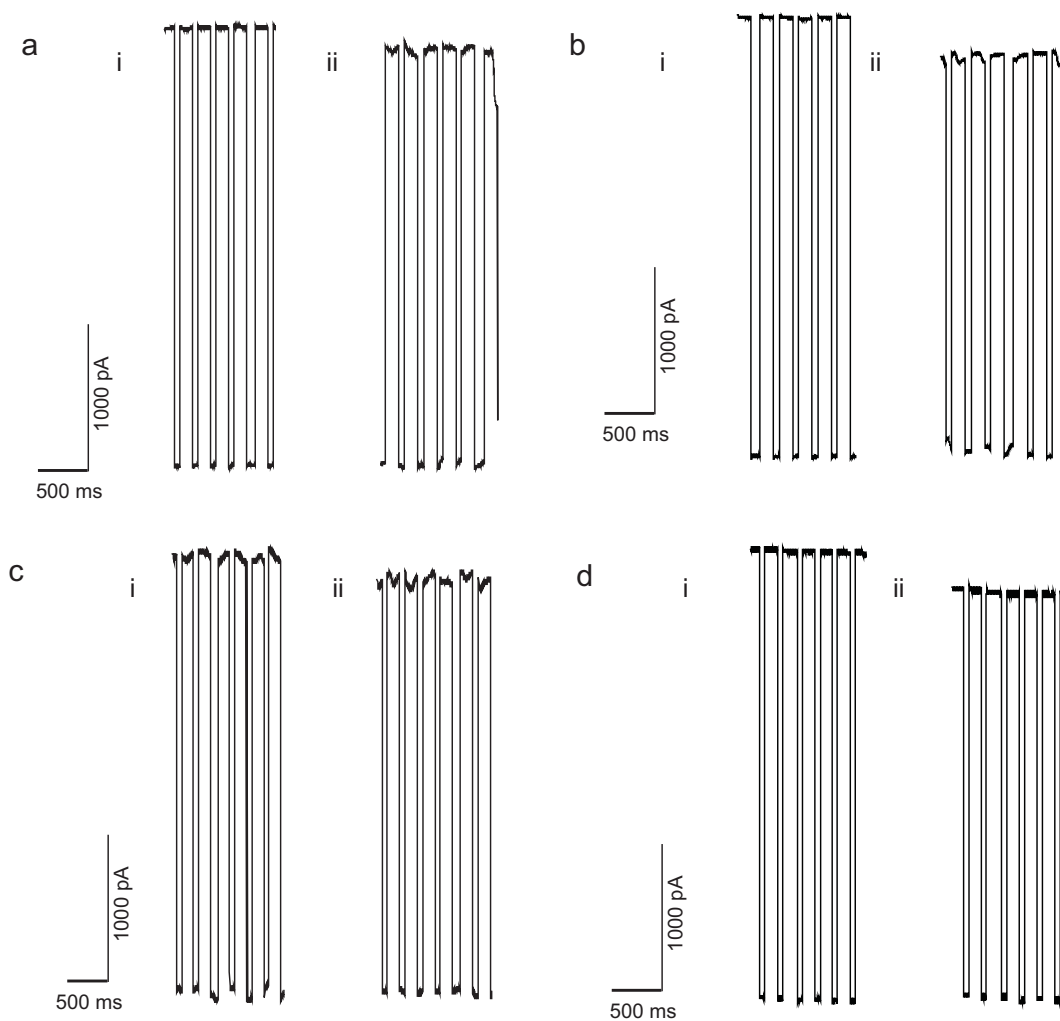


f



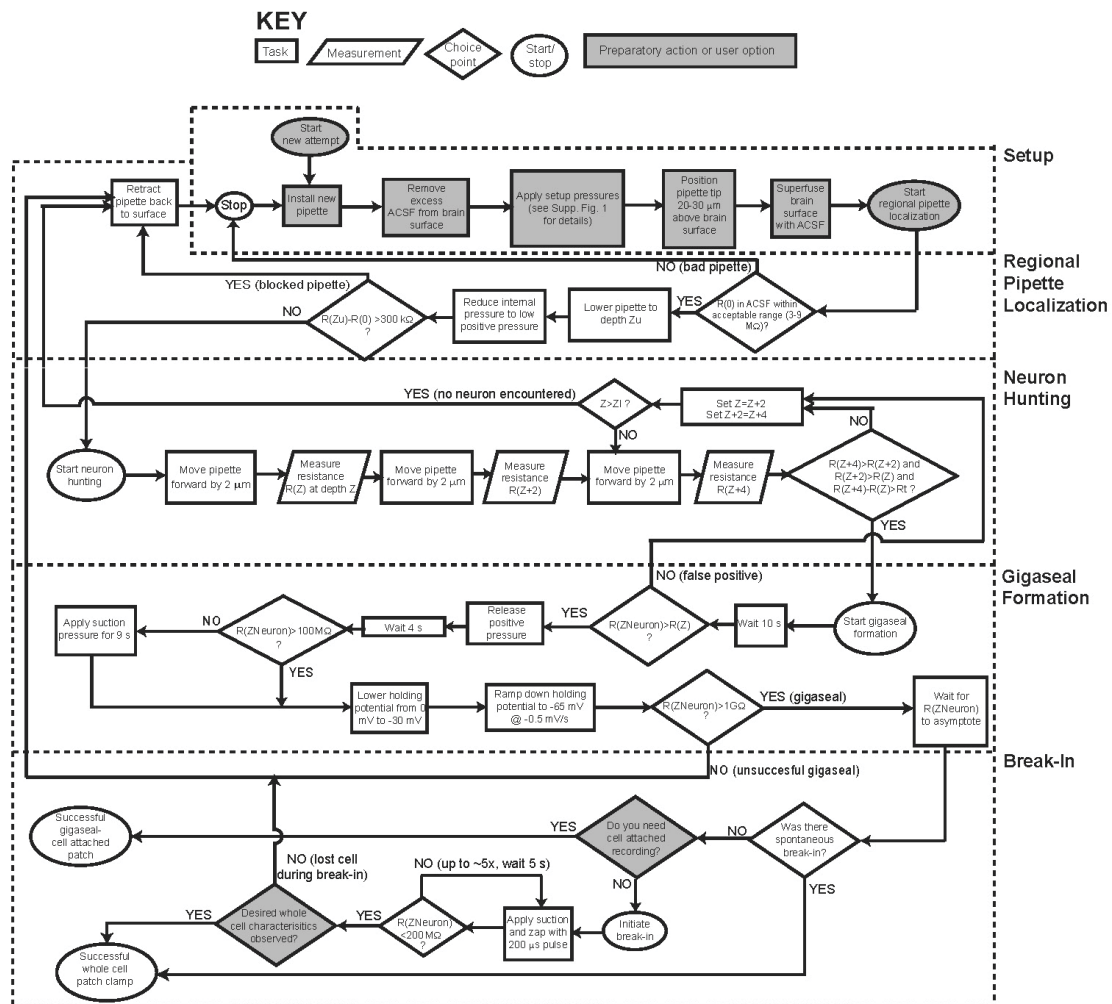


**Supplementary Figure 1. Details of Autopatcher setup** (a) Diagram depicting configurations of the three pneumatic valve banks during the stages of autopatcher operation, depicted in **Fig. 1a** and **Supplementary Fig. 3**. “x” represents closed valve; line depicts connectivity of volumes at the same pressure. **Left**, during regional pipette localization, positive pressure (800-1,000 mBar) is connected to the pipette. (This is the configuration realized when the valves are not powered.) **Center**, during neuron hunting, low positive pressure (25-30 mBar) is connected to the pipette. **Right**, during gigaseal formation, suction pressure (−15 to −20 mBar; dotted line) or atmospheric pressure (solid line) is applied. During break-in, suction pressure is also applied. (b) Photograph of the Autopatcher setup, focusing on three axis linear actuator (here, with an additional programmable linear motor appended, for ease of debugging) and the holder for head-fixing the mouse.



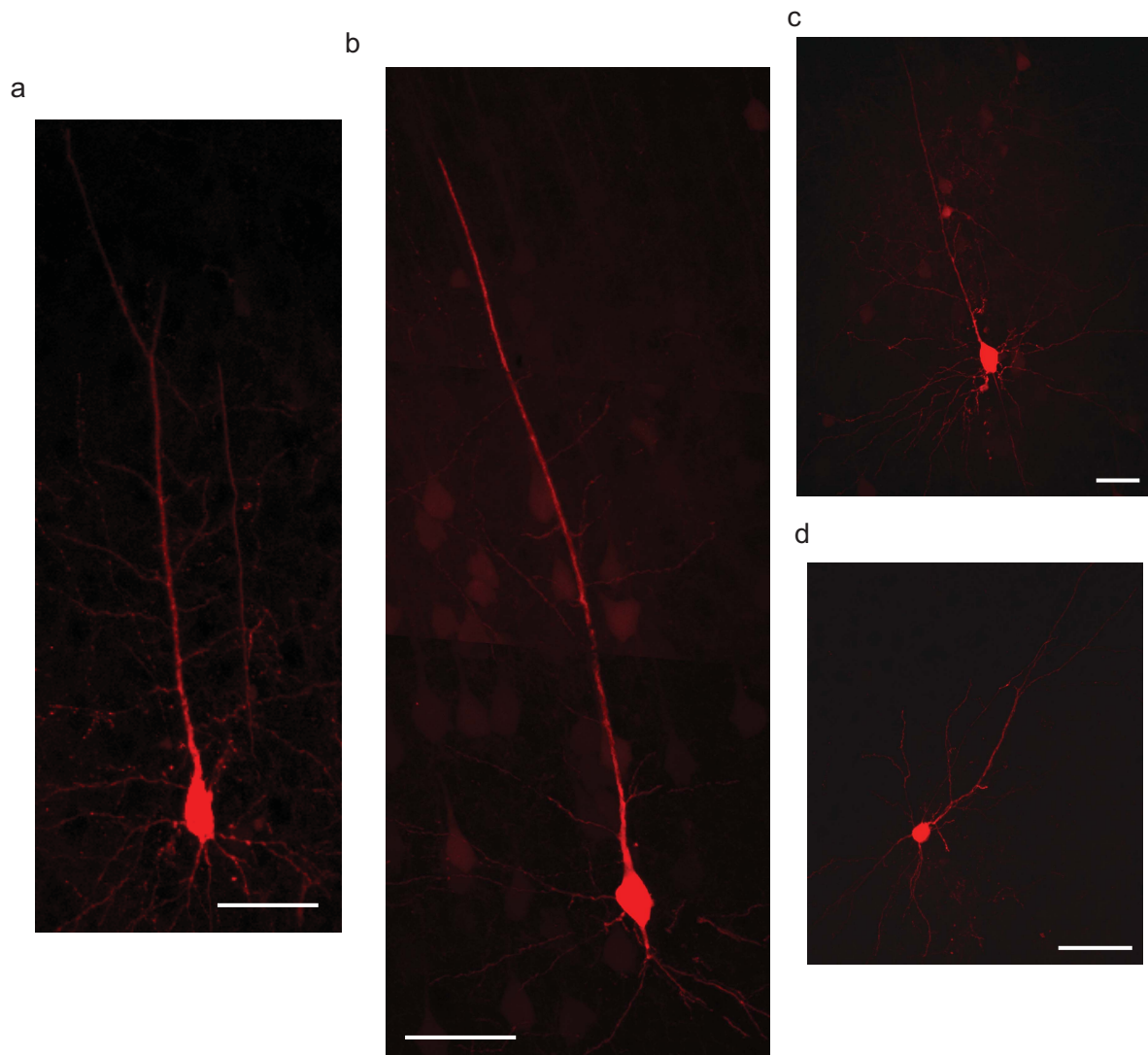
**Supplementary Figure 2. Raw current traces recorded during “neuron hunting” stage.**

Shown are patch pipette currents obtained when a square voltage wave (10 Hz, 10 mV during “neuron hunting” stage) is applied to the pipette in voltage clamp mode. The *left* traces in **a-d** are current traces measured 10  $\mu\text{m}$  before the pipette was stopped at the end of “neuron hunting” to attempt “gigasealing”. The *right* traces in **a-d** are current traces measured at the point the pipette was stopped at the end of neuron hunting. Trials **a-c** culminated in successful whole cell patch clamp recording, while **d** did not result in successful gigaseal, and subsequently was unsuccessful in establishing whole cell as well. Comparing the successful trials, while the *left* traces in **a** and **b** show no heart beat modulation at distance from the neuron, the *left* trace in **c** shows heart beat modulation of the current traces even 10  $\mu\text{m}$  away from point of stoppage. The *right* traces in **a-c** all show prominent heart beat modulation at the point of stoppage; this is not seen in the *right* trace in **d**.

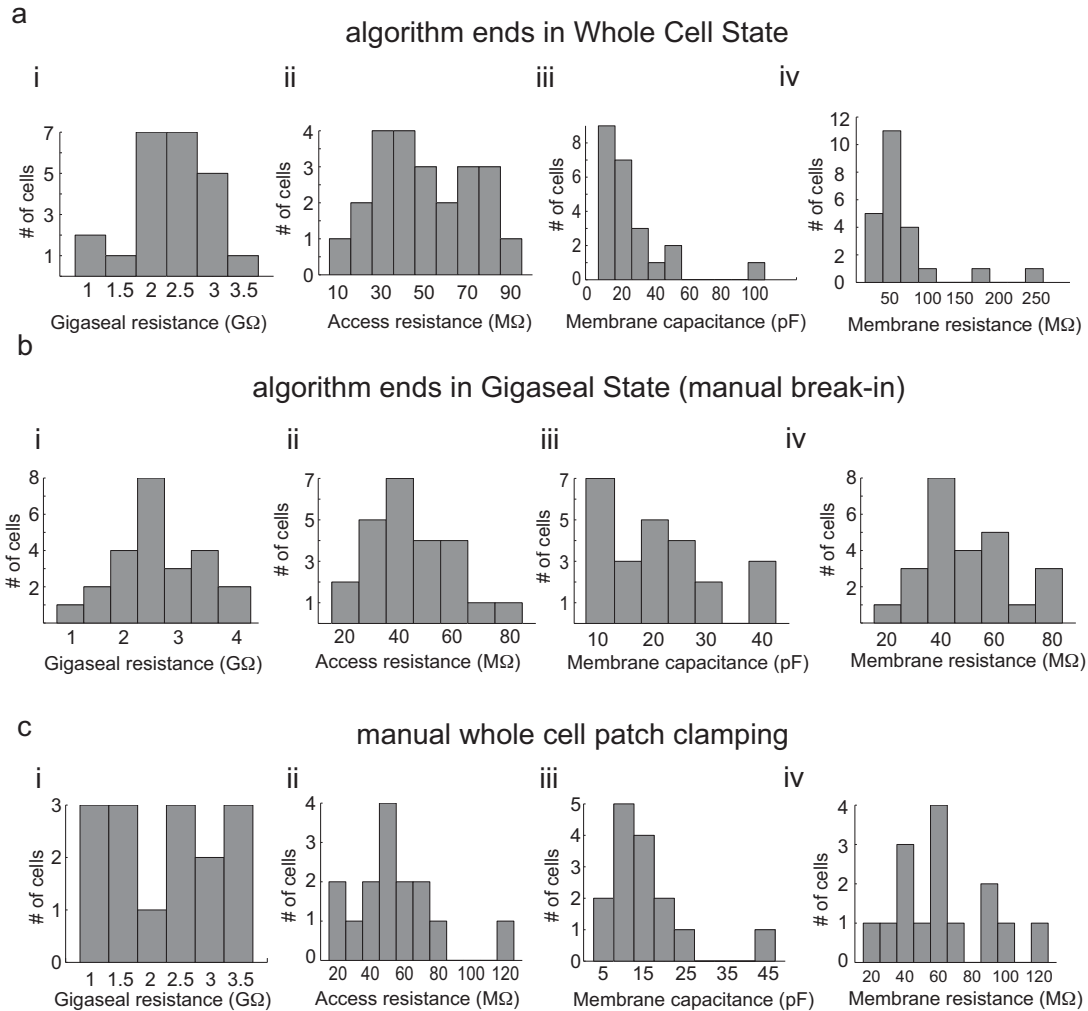


### Supplementary Figure 3. The full algorithm for automated *in vivo* patch clamping.

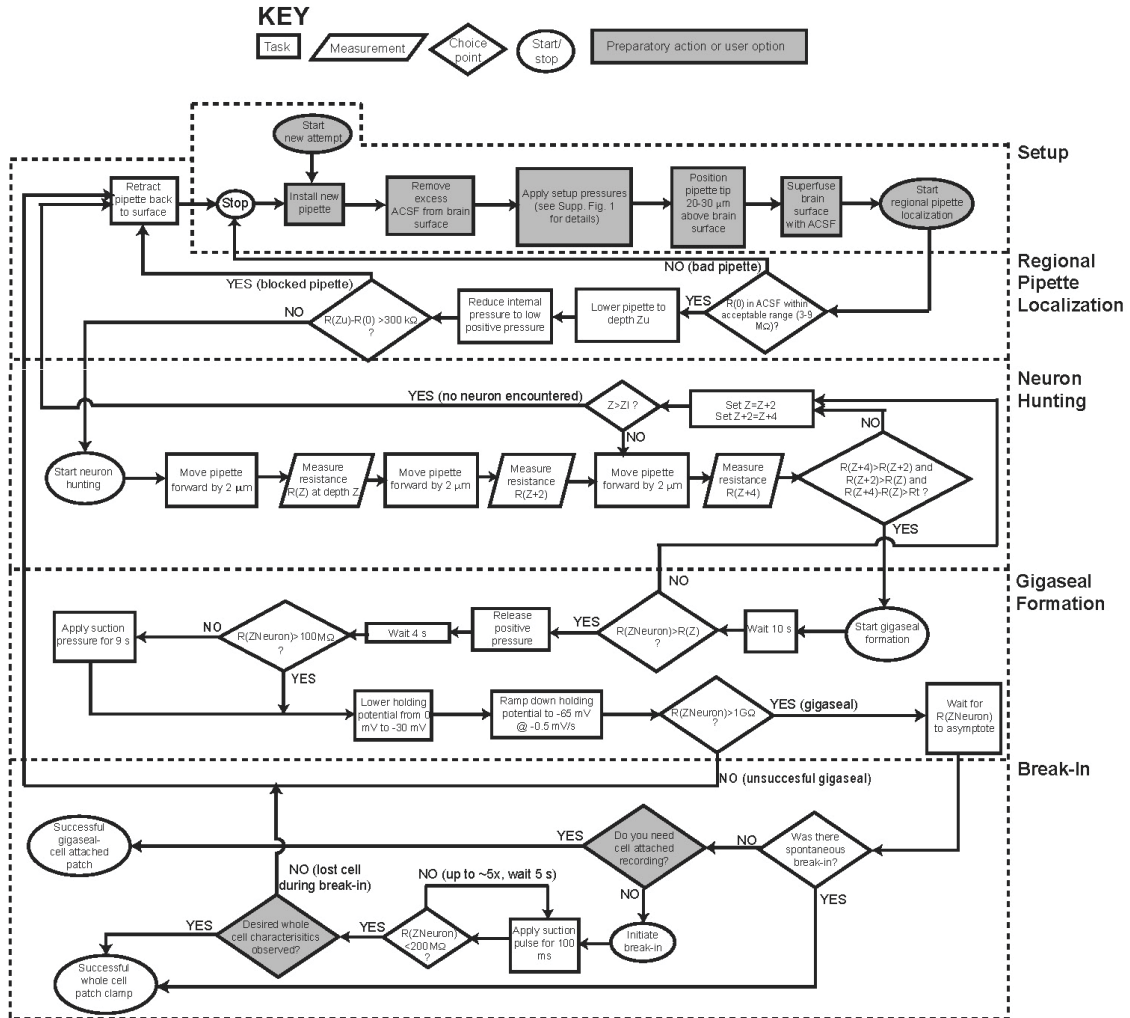
Detailed flowchart, showing all steps for the automated *in vivo* patch process, including strategies for stage execution, and quantitative milestones governing process flow and decision making. Dotted lines frame each of the stages of the algorithm; within the dotted line frames, symbols representing tasks, measurements, and choice points are indicated, along with text explicating the individual steps and consequences of decisions (see “KEY” for definition of symbols). Abbreviations: ACSF, artificial cerebrospinal fluid;  $R(Z)$ , pipette resistance at depth  $Z$  in the brain, in microns (with the  $z$ -axis pointing downward, e.g. larger values of  $Z$  indicate deeper targets);  $Z_u$ , upper depth limit of the region targeted by the regional pipette localization stage;  $Z_l$ , lower depth limit of the region targeted by the regional pipette localization stage;  $R(Z_{Neuron})$ , pipette resistance at the depth at which the neuron is being recorded (which will vary over time, as the later stages of the process, gigasealing and breaking-in, occur);  $R_t$ , pipette resistance threshold for neuron detection. See Supplementary Fig. 1 for the valve states at specific stages of the algorithm.



**Supplementary Figure 4. Neurons filled with biocytin, and visualized with Alexa 594-streptavidin, after recording by the autopatching robot.** Each panel shows a neuron recorded at 500-800  $\mu\text{m}$  depth below the brain surface, 0-2 mm left or right of midline, 0-2 mm anterior of bregma. Scale bars, 50  $\mu\text{m}$ .

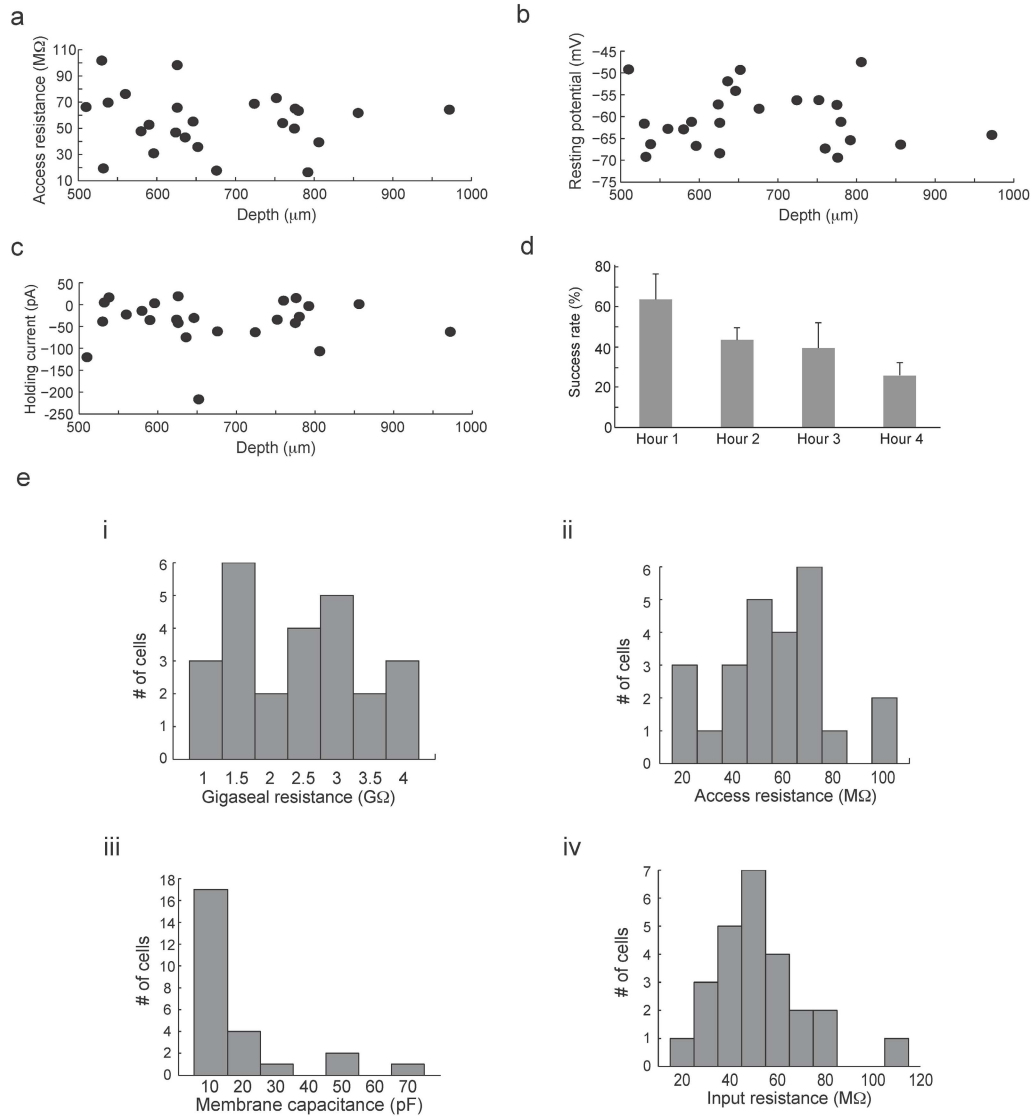


**Supplementary Figure 5. Cell characteristics after completion of autopatching or manual patching using the algorithm of Supplementary Fig. 3.** Histograms summarizing the whole cell patch clamp properties of the neurons described in **Figure 2** for which recordings were either automatically established in **(a)** whole cell state ( $n = 23$  cells), or **(b)** gigaseal state followed by manual break-in to verify cell properties ( $n = 24$  cells), or **(c)** fully manual whole cell patch clamping ( $n = 15$  cells), measured in voltage clamp at  $-65$  mV, including **i**, gigaseal resistance after gigaseal formation, **ii**, access resistance after break-in ( $\sim 5$  minutes after break-in), **iii**, cell membrane capacitance, and **iv**, cell input resistance.



**Supplementary Figure 6.** The algorithm of Supplementary Fig. 3, modified to use suction pulses instead of “zap” (see differences in the “Break-In” phase of this figure, compared to that of Supplementary Figure 3), to break in. The algorithm for automated *in vivo* patch clamping when using “suction pulses” for the break-in stage, rather than “zap,” to establish the whole cell state. All symbols, shadings, headers, etc. are as in Supplementary Fig. 3.





**Supplementary Figure 7. Quality of recordings obtained using the autopatcher using the ‘suction pulses’ method for break-in and achieving the whole cell state, as described in Supplementary Fig. 6.** (a) Plot of the access resistances obtained versus pipette depth for set of neurons for which whole cell state was established using the algorithm of **Supplementary Fig. 6**, in which the “zap” is replaced by suction pulses.  $n = 25$  cortical neurons were successfully broken in to, out of 30 successful gigaseals, out of 61 total attempts starting with regional pipette localization (anteroposterior, 0 mm relative to bregma; mediolateral, 0-1 mm left or right of the midline; neuron hunting begins at 400 μm depth). Thus the break-in rate was 83% of the gigasealed neurons (not different from the break-in rate for zap-mediated break in, **Fig. 1a**; chi-square = 0.001,  $P = 0.8023$ ), and total yield from start of the algorithm was 41%. (b) Plot of the resting potentials obtained versus pipette depth, for the neurons described in a. (c) Plot of the holding currents obtained versus pipette depth for the neurons described in a. The recordings lasted at least 15 minutes, but we terminated the recordings early in order to focus more on the understanding of whether suction pulses would work in the autopatcher algorithm. (d) Bar graph



of average success rates obtained in each hour of recording after surgery ( $n = 3$  experimental sessions; plotted is mean + standard deviation). (e) Histograms summarizing the whole cell properties of the automatically whole-cell patched neurons broken in using suction pulses method, showing good quality recordings equivalent to those obtained by zap method of break-in, measured in voltage clamp at  $-65$  mV, including **i**, gigaseal resistance after gigaseal formation, **ii**, access resistance after break-in ( $\sim 5$  minutes after break-in), **iii**, cell membrane capacitance, and **iv**, cell input resistance.

	Regional Pipette Localization	Neuron Hunting	Gigaseal Formation	Break-In
%age yield, whole cell patch	81%	93%	51%	82%
%age yield, gigaseal cell-attached	80%	93%	41%	N.A
Duration of stage (mean $\pm$ s.d.)	10 s	2.2 $\pm$ 1.7 min	2.6 $\pm$ 1.0 min	1-10 s

**Supplementary Table. 1:** Yields and durations of each of the four stages, when executed by the robot of **Fig. 1b**, running the autopatching algorithm in the living mouse brain, aiming for targets in cortex and hippocampus (fully automated successful attempts defined as  $< 500$  pA of current when held at  $-65$  mV, for at least 5 minutes;  $n = 24$  out of 73 attempts, successful gigaseal cell-attached patch clamp recording defined as a stable seal of  $> 1$  G $\Omega$  resistance;  $n = 27$  out of 75 attempts).

### **Supplementary Note 1. Derivation of the autopatcher algorithm: principles of whole cell patch clamp *in vivo***

We derived the autopatcher algorithm (**Supplementary Fig. 3**) by analyzing and optimizing successively each of the four stages of robot operation (**Fig. 1a**). Importantly, the algorithm derivation described below was performed completely in the cortex, but the testing of the algorithm was performed on both cortical neurons as well as hippocampal neurons. This generalization of the algorithm from cortex to hippocampus implies that the algorithm possesses a certain degree of generalization power, i.e., we did not unconsciously optimize the algorithm just for one brain region. Nevertheless, it is likely that specialized neurons in novel brain regions may require tuning of select algorithm parameters, and the ability to perform this optimization using the robot would accelerate this process of customization, allowing for rapid iteration beginning from the parameters derived here. We also tested the autopatcher on brain slices, where it was capable of obtaining good recordings.

At the beginning of the algorithm (gray flowchart shapes in the “setup” stage at top of **Supplementary Fig. 3**), a pipette is placed in the holder and provided strong positive pressure, and the robot then (stage 1, “regional pipette localization”) lowers the pipette at a speed of  $200 \mu\text{m/s}^{1-5}$  to the appropriate depth for neuron hunting. We found, as have others before us, that using reasonably strong positive pressure (800-1,000 mBar)<sup>9, 11, 6</sup> greatly improved the yield of subsequent stages. For experiments where we performed biocytin staining, we explored using 500-600 mBar of pressure in this stage, to reduce the amount of biocytin ejected during “regional pipette localization,” and thus potentially the background staining of biocytin on non-patched neurons; this did not seem to have much effect, but such detailed modulations of pipette positive pressure over time may be worth exploring further in future algorithms. Another key finding was that after this first localization stage was complete, many pipettes had slightly increased their resistances over their original values. Pipettes that acquired greater increases in resistance

in this first stage had, in later stages of robot operation, more variability in their pipette resistance measurements than pipettes with smaller increases. For example, the variance between successive measurements of pipette resistance across multiple steps taken during the “neuron hunting” stage was  $87 \pm 60 \text{ k}\Omega$  for pipettes that experienced zero increase in resistance acquired during the first localization stage, but was  $218 \pm 137 \text{ k}\Omega$  for pipettes that experienced 500  $\text{k}\Omega$  increases, significantly more variability (mean  $\pm$  s.d. ;  $p < 0.05$ , t-test,  $n = 7$  trials each). By screening out pipettes that underwent large increases in pipette resistance during the first localization stage, the variability of pipette resistance measures in successive stages of robot operation can be reduced, improving the accuracy of the subsequent stages. We found that by excluding pipettes that increased resistance by more than 300  $\text{k}\Omega$  in the first localization stage (which would result in a  $136 \pm 83 \text{ k}\Omega$  measurement-to-measurement variance in the neuron hunting stage;  $n = 123$  trials),  $\sim 17\%$  of the pipettes would be discarded ( $n = 25$  out of 148 total attempts in the main robot validation test set; **Fig. 1a**), but because of the low variability of later pipette resistance measurements, it became possible to detect neurons very precisely, as indicated by well-defined increases in pipette resistance, during the neuron hunting stage (stage 2).

In published neuron hunting protocols, a visually identified increase of 20-50% in pipette resistance was considered to be indicative of the presence of a viable neuron, appropriate for attempting gigaseal and break-in stages<sup>1,2,4</sup>. One advantage of a robotic system is that it can analyze sequences of pipette resistance values acquired over a series of successive motor steps, thus enabling precise signatures of neuron presence that algorithmically replicate the intuitive comparisons being performed by trained human investigators. We systematically explored this parameter space, varying the number of consecutive 2  $\mu\text{m}$  steps over which pipette resistance values would be considered, and also varying the numerical threshold that the pipette resistance would have to increase over these steps in order for a neuron detection to be concluded, aiming to maximize the success of manually establishing whole-cell patch clamping for each neuron-hunting procedure. We found analysis of only 2 consecutive motor steps (i.e., pipette resistance data over 4  $\mu\text{m}$  of travel) to yield noisy data, and 4 consecutive steps (i.e., over 8  $\mu\text{m}$  of travel) to detect the neuron too late to get good recordings, perhaps because the cell was stretched. Thus, we focused our analysis on pipette resistance sequences taken over 3 consecutive steps (6  $\mu\text{m}$ ). Because the measurement-to-measurement variability on consecutive motor steps (see above) was about 136  $\text{k}\Omega$ , we chose to investigate thresholds of pipette resistance increase between the first and third step of 150, 200, 250, 300, 350, and 400  $\text{k}\Omega$ . We found that first-to-third step differences of at least 200-250  $\text{k}\Omega$  yielded patchable neurons at success rates of 40-45% ( $n = 11$  cells out of 25 were manually successfully gigasealed and broken-into). In contrast, 3-step sequences with  $< 200 \text{ k}\Omega$  thresholds or  $> 300 \text{ k}\Omega$  thresholds had much lower success rates of manual gigasealing and breaking-into (5-15% yields; 4 out of 27), perhaps due to errors in neuron detection or approach (false positives for the lower thresholds; cell stretching for the higher thresholds). Thus, we chose for the robot a 200  $\text{k}\Omega$  threshold for pipettes of 3-5  $\text{M}\Omega$  initial resistance, and 250  $\text{k}\Omega$  for pipettes of 5-9  $\text{M}\Omega$  initial resistance. In the main robot validation test set we found that this neuron hunting algorithm converged upon targets within the localized region 93% of the time (114 targets detected out of 123 total trials); of these 114, 56 cells ultimately resulted in a gigaseal, or a yield of 49% - similar to the 40-45% rate obtained during the pilot studies using manual validation, mentioned earlier in this paragraph.

For comparison purposes, we evaluated the value of observing heartbeat modulation as an indication of neuronal detection. According to ref. <sup>4</sup>, *“The best predictor of the pipette having made contact with a neuronal membrane was pulsation of the reduced current pulse at heartbeat frequency... Slow changes in current pulse amplitude that lacked the rhythmic modulation rarely resulted in neuronal recordings... one of the trademark characteristics of the ‘strike’ of the pipette against neuronal material is pulsation of the recorded current at heartbeat frequencies. In our experience this is the best indicator of the patch pipette making contact with neuronal material. While there were instances in which this pulsation was due to contact with non-neuronal membranes, presumably glia or blood vessels, this occurred less than 5% of the time.”* In order to determine whether heartbeat modulation of pipette currents was also a good indicator of neuronal detection in our hands, we used the autpatching robot to record  $n = 17$  neurons, keeping attuned to the presence or absence of heartbeat modulation. All 17 neurons patched exhibited, at the point of completion of the “neuron hunting” stage, a prominent heartbeat modulation (see **Supplementary Fig. 2a-c** for examples), in full accordance with the Margrie et al. paper. Thus, in principle, heartbeat modulation could be added as a confirmatory check in the algorithm, although we did not find it necessary; it appears that our algorithms’ search for a monotonically increasing pipette resistance recapitulates the same essential process that takes place in the heartbeat detection procedure.

We note that we often saw heartbeat modulation sometimes, but not always, when the patch pipette was 10  $\mu\text{m}$  away from the neuron (e.g., five 2  $\mu\text{m}$  steps before the pipette halted and the “neuron hunting” stage ended; **Supplementary Figs. 2c**); this occurred 6 out of the 17 times, and may indicate that heartbeat modulation may occur even before the pipette resistance increases, and thus when a neuron has not been quite detected. (This neuron-selectivity that our algorithm encapsulates may explain why  $\sim 90\%$  of the structures we patched were neuronal, with only  $\sim 10\%$  glial, as noted in the main text. Why so few glia and non-excitable structures? It is possible that we are actually encountering a lot of these, but we are not sealing well on to them with our current pipette shape and search algorithm. Remember, although most of the cells we patched indeed were neurons (see **Supplementary Note 2** below) – the patch algorithm did not form good gigaseals typically  $\sim 50\%$  of the time – and those targets may be with connective tissue, glia, blood vessels, etc. This is consistent with the strong neuron selectivity of papers such as ref. <sup>5</sup>, as mentioned above.) Notably; we also analyzed  $n = 26$  attempts in which neuron hunting halted on an object (perhaps a cell, or a piece of connective tissue), but which did not yield a gigaseal (e.g., **Supplementary Fig. 2d**); in 24 such cases (such as the one shown in **Supplementary Fig. 2d right**), there was no heartbeat modulation; in the remaining two cases, extreme heartbeat modulation was seen (perhaps suggesting a blood vessel to be there). Thus again, heartbeat modulation could be used to confirm our algorithm, but given the complexity in automating heartbeat modulation analysis (heartbeat, after all, varies greatly in shape and frequency from cell to cell, mouse to mouse, and depending on anesthesia protocol), we decided to stick with the simpler-to-automate monotonic pipette resistance\_criterion for our algorithm. It is possible, however, given our independent confirmation of the heartbeat modulation criterion, that heartbeat modulation, given its prominent visual pattern, is still one of the best methods for human use for neuron detection. In principle, future versions of the algorithm that take heartbeat modulation into account, might enable failed gigaseal trials to be ended early, thus saving several seconds per cell of time, and speeding up the robot still more.

The gigaseal formation stage (stage 3) was adapted from the best practices of prior protocols, aiming for a stereotyped sequence of steps amenable to automation. The motor was switched off after neuron hunting completion, and a 10 second wait period was imposed to see if the pipette resistance decayed back to baseline (this happened 1 time out of the 114 successful hunts; the motor simply reactivated and the neuron-hunting stage resumed). Then the positive pressure was released, suction pressure was applied if the gigaseal was not spontaneous, and the holding potential was reduced slowly to  $-65$  mV (see **Supplementary Fig. 3**, “gigaseal formation” for the detailed series of steps). If a gigaseal was not apparent at the end of this procedure, the algorithm was halted (although, these could be considered loose-cell attached patches – of interest because of the excellent single cell isolation offered, even if subthreshold and synaptic events are not observable as in the whole-cell case); else, the gigaseal was left until it plateaued for at least 10-15 seconds (see **Fig. 2a** for example). In the main robot validation test set, of the 114 targets detected by “neuron hunting”, 56 formed gigaseals (49% yield) under the operation of the robot.

The final stage was break-in (stage 4), and again, we aimed for a procedure that would be easily and objectively automated. The robot applied suction for periods of 1 second, and then precisely activated the “zap” function of the patch amplifiers (a  $200$   $\mu$ s voltage pulse to  $1$  V), repeatedly every 5 seconds until the whole-cell configuration was obtained. In this scenario, we reserved the judgment of the whole cell state for a human observer, who could then halt the program, because we were seeking to analyze the quality of our recordings; the stereotyped changes in the recording due to the cell capacitance and resistance being appended to the pipette are also quantifiable (**Supplementary Fig. 5**) to the extent of yielding automation of program cessation, if desired. As a comparison, we have also included fully manually patched recording quality data. In practice, only a few zaps were needed, to establish whole cell state, so break-in could in principle be conducted in an open-loop fashion if desired. In the main robot validation test set, the 56 gigasealed neurons were split into three sets: 5 underwent spontaneous break-in without human or robot interference (thus counted as automated-whole-cell-attached trials), 24 underwent break-in using the robot, and 27 were manually broken-into in order to evaluate the success of our automated break-in procedure. Out of the 24 automatically broken-in trials, 19 successfully attained whole-cell mode (79% success); failures (5 cells) were stringently defined as a lack of break-in, “losing” the cell within 5 minutes of attaining whole-cell recording, or exhibiting  $>500$  pA of holding current (at  $-65$  mV). Including the trials where spontaneous break-in occurred to this dataset, we were able to get automated whole-cell-attached recordings, that met the success criteria described above 83% of the time ( $n = 24/29$ ). For the 27 other cells, we achieved manual whole-cell break-in in 100% of the cells using standard methods, applying brief suction pulses in rapid succession<sup>1</sup>. It is clear that the objective and systematic analysis of how *in vivo* patch clamping occurs, coupled to precision measurement and well-timed robotic control of pipette movement and pressure control, enables automation of the steps at which humans ordinarily require extensive practice to master.

Further, we incorporated a second method of automated *in vivo* patching using suction pulses to achieve the break-in step (algorithm described in **Supplementary Fig. 6**, data shown in **Supplementary Fig. 7**). Once the gigaseal is established, the experimenter needs to manually increase the suction pressure in the suction port (**Fig. 1**, **Supplementary Fig. 1**) to  $-30$  to  $-50$  mBar; alternatively, an additional valve and an additional pressure source could be utilized.

When activated, the robot applies suction for a period of 100 ms, repeatedly, every 5 seconds, until whole cell configuration is established. Out of the 30 trials where the ‘suction pulse’ method was employed to break-in, 25 successfully attained whole-cell mode (83.3%).

In the biocytin filling experiments, we recorded and filled 5 neurons (shown in **Fig. 1f**, **Supplementary Fig. 4**) that we held for > 15 minutes in voltage clamp mode, using the criterion < -500pA of current injection to hold at -65 mV throughout the length of the recording. We wrote a second program that simply, after this period, retracts the pipette at a constant speed of 3  $\mu\text{m/s}$  (see **User Manual** for details) to attempt to form an outside out patch, to result in a good fill (i.e., trapping the biocytin in the cell)<sup>7</sup>.

### **Supplementary Note 2. The cell types patched by the autopatcher**

Using the cell type criteria of references<sup>8,9</sup>, we found that of the 47 autopatched neuronal recordings from cortex and hippocampus analyzed in **Fig. 2** and **Supplementary Fig. 5a,b**, 68% (32/47) exhibited regular spiking (RS) characteristics, 4% (2/47) exhibited burst firing patterns, 13% (6/47) exhibited irregular spike characteristics, 4% (2/47) exhibited spikes followed by smaller spikelets suggestive of back propagation of action potentials in dendritic recordings, and 2% (1/47) had accelerating spike firing characteristics. In 9% (4/47) of the neurons, steady current injection resulted in a single action potential followed by plateaued depolarizing current, with no further spike firing, indicating fast adapting neurons. It is likely that all cell recording strategies have some bias in what kinds of cells they record; extracellular recording methods, for example, might favor neurons capable of creating large extracellular fields that result in easily sortable spikes for example (papers such as ref.<sup>10</sup> comment on how difficult it is to record small neurons like cerebellar granule cells via extracellular recording). A recent *in vivo* patch clamping paper, ref.<sup>11</sup> points out, “*Most of the recorded cells were pyramidal cells and their recovered morphologies typically included an apical dendrite ...*”, which would be consistent with our apparent high yield of neurons, especially pyramidal neurons, as noted in this paragraph and in the fills (**Supplementary Fig. 4**).

### **Supplementary Note 3. Statistics for evaluation of cell quality, for autopatched neurons**

We analyzed both the cell quality (**Fig. 2c-f**) for both neurons automatically patched in whole cell mode, and neurons patched in gigaseal cell-attached mode, in the main robot validation test set ( $n = 47$  successful neurons); the latter were then manually broken into in order to assess critical measures of cell and recording quality. No difference in access resistances was noted between cortex vs. hippocampus, or between auto-whole-cell patched and the auto-cell-attached-patched plus manual break-in (two-way ANOVA; main effect of region,  $F_{1,45} = 0.0038$ ,  $P = 0.9534$ ; main effect of break-in mode,  $F_{1,45} = 1.5107$ ,  $P = 0.2056$ ; interaction,  $F_{1,45} = 0.7533$ ,  $P = 0.3583$ ). We performed a linear regression of pipette access resistance vs. neuron recording depth, and saw no relationship ( $R^2 = 0.007$ ,  $P = 0.0806$ ), suggesting that our robot performed similarly at depth as at the surface.

### **Supplementary Note 4. Statistics for comparing cell quality of autopatched neurons with fully manual patched neurons**

Comparing the cell quality metrics between the  $n = 23$  auto-whole cell patched neurons and the 15 *fully* manually patched neurons (**Figs. 2c-f**, **Supplementary Fig. 5**): No difference between auto-whole-cell patched and fully manually patched neurons was noted for access resistances



(two-way ANOVA; main effect of method of patching,  $F_{1,33} = 0.92$ ,  $P = 0.5116$ ; main effect of region (cortex vs hippocampus),  $F_{1,33} = 1.73$ ,  $P = 0.4175$ ; interaction,  $F_{1,33} = 0.14$ ,  $P = 0.706$ , holding current (two-way ANOVA; main effect of method of patching,  $F_{1,33} = 0.83$ ,  $P = 0.5382$ ; main effect of region,  $F_{1,33} = 0.12$ ,  $P = 0.7819$ ; interaction,  $F_{1,33} = 0.38$ ,  $P = 0.5432$ ), or resting membrane potential (two-way ANOVA; main effect of method of patching,  $F_{1,33} = 1.16$ ,  $P = 0.4758$ ; main effect of region,  $F_{1,33} = 0.72$ ,  $P = 0.5539$ ; interaction,  $F_{1,33} = 5.873$ ,  $P = 0.0218$ ). Out of the 47 neurons from which we obtained stable recordings, we terminated 14 recordings early (30-45 minutes) in order to try for more cells; for the remaining 33 cells, the recordings lasted  $56.6 \pm 44.2$  minutes (**Fig. 2F**). No difference in cell holding times was noted between auto-whole-cell patched and fully manually patched neurons (two-way ANOVA; main effect of method of patching,  $F_{1,33} = 3.19$ ,  $P = 0.3279$ ; main effect of region,  $F_{1,33} = 0.19$ ,  $P = 0.7317$ ; interaction,  $F_{1,33} = 1.08$ ,  $P = 0.3016$ ). Finally, no difference between auto-whole-cell patched and fully manually patched neurons was noted for gigaseal resistance (two-way ANOVA; main effect of method of patching,  $F_{1,33} = 1.85$ ,  $P = 0.1809$ ; main effect of region,  $F_{1,33} = 0.12$ ,  $P = 0.7267$ ; interaction,  $F_{1,33} = 6.02$ ,  $P = 0.0192$ ), cell membrane capacitance (two-way ANOVA; main effect of method of patching,  $F_{1,33} = 0.96$ ,  $P = 0.9578$ ; main effect of region (cortex vs. hippocampus),  $F_{1,33} = 2.91$ ,  $P = 0.09628$ ; interaction,  $F_{1,33} = 0.7$ ,  $P = 0.4021$ ), or cell input resistance (two-way ANOVA; main effect of method of patching,  $F_{1,33} = 1.47$ ,  $P = 0.2327$ ; main effect of region,  $F_{1,33} = 0.25$ ,  $P = 0.2417$ ; interaction,  $F_{1,33} = 0.06$ ,  $P = 0.8182$ ).

### Supplementary Note 5. Thoughts on throughput of the autopatcher

Is the autopatcher a “high throughput” machine? Perhaps, but not in terms of sheer speed per cell (currently), although certainly the autopatcher can sustain its work without getting tired or bored, as a human might. We did a series of experiments, automatically recording in each of 3 mice, 7-8 successfully whole cell patch clamped neurons (total for the 3 mice, 22 successes), out of 16-20 attempts (total for the 3 mice, 52 attempts; yield, 42%); surgeries would take  $41 + 6$  minutes beginning from anesthesia of the mouse and ending with the exposed brain ready for recording; then, for each cell, pipette filling and installation (removing any used pipette, of course) would take  $2 \pm 0.4$  minutes, followed by the autopatcher establishing whole cell patch clamp in  $5 \pm 2$  minutes. We limited the recording time for each cell to 15 minutes, arbitrarily, but shorter or longer times may be of course utilized, depending on the science at hand. Thus, the amount of time required to record  $n$  neurons successfully, for a desired recording time  $T$ , would be approximately

$$40 + n / .42 * 7 + n / .42 * T$$

minutes. (The surgeries, of course, could be done in advance to equip mice with headplates to minimize day-of-recording time expenditure.) Thus, during an 8 hour day, ~25 neurons might be successfully recordable in a single mouse, if the recording times were very short; this doesn't take into account the important consideration of cell displacement (e.g., see **Supplementary Fig. 7d**) that could result from an electrophysiological experiment, thus reducing yield over time.

Strategies can be devised to limit the impact of cell displacement or damage from impacting yield, for example, patching neurons in higher regions before patching those in lower ones. The autopatcher travels, on average,  $150 \pm 112$  microns in the cortex during the neuron hunt phase, before hitting the neuron ( $n = 22$  cells); this short travel distance suggests that the pipette might well be hitting the very first cell that it is allowed to encounter (e.g., is approaching under low pressure). Smaller diameter pipettes, even down to 100-200 microns in diameter, are easily

available (albeit more difficult for humans to handle), and so this might not be a fundamental limit on scale. Or, it is possible that patching neurons in varying brain regions could result in very high fidelity recordings, although again, the science would have to match with this goal.

Also important to note: if it takes 2 minutes to load a pipette, and 5 to obtain a cell and another T minutes to do a recording, it would in principle be possible for a single individual to run  $(5+T)/2$  rigs at once; for 15 minute recording times, that would make for 10 rigs being simultaneously controlled by one employee.

#### SUPPLEMENTAL REFERENCES

1. DeWeese, M.R. Whole-cell recording in vivo. *Curr Protoc Neurosci* **Chapter 6**, Unit 6 22 (2007).
2. Harvey, C.D., Collman, F., Dombeck, D.A. & Tank, D.W. Intracellular dynamics of hippocampal place cells during virtual navigation. *Nature* **461**, 941-946 (2009).
3. Lee, A.K., Manns, I.D., Sakmann, B. & Brecht, M. Whole-cell recordings in freely moving rats. *Neuron* **51**, 399-407 (2006).
4. Margrie, T.W., Brecht, M. & Sakmann, B. In vivo, low-resistance, whole-cell recordings from neurons in the anaesthetized and awake mammalian brain. *Pflugers Arch* **444**, 491-498 (2002).
5. Margrie, T.W. et al. Targeted whole-cell recordings in the mammalian brain in vivo. *Neuron* **39**, 911-918 (2003).
6. Margrie, T.W., Brecht, M. & Sakmann, B. In vivo, low-resistance, whole-cell recordings from neurons in the anaesthetized and awake mammalian brain. *Pflugers Arch* **444**, 491-498 (2002).
7. Rancz, E.A. et al. Transfection via whole-cell recording in vivo: bridging single-cell physiology, genetics and connectomics. *Nat Neurosci* **14**, 527-532 (2011).
8. Degenetais, E., Thierry, A.-M., Glowinski, J. & Gioanni, Y. Electrophysiological Properties of Pyramidal Neurons in the Rat Prefrontal Cortex: An In Vivo Intracellular Recording Study. *Cerebral Cortex* **12**, 1-16 (2002).
9. Petilla terminology: nomenclature of features of GABAergic interneurons of the cerebral cortex. *Nat Rev Neurosci* **9**, 557-568 (2008).
10. Chadderton, P., Margrie, T.W. & Hausser, M. Integration of quanta in cerebellar granule cells during sensory processing. *Nature* **428**, 856-860 (2004).
11. Rancz, E.A. et al. Transfection via whole-cell recording in vivo: bridging single-cell physiology, genetics and connectomics. *Nat Neurosci* **14**, 527-532 (2011).
12. Lee, A.K., Epsztein, J. & Brecht, M. Head-anchored whole-cell recordings in freely moving rats. *Nat. Protocols* **4**, 385-392 (2009).